Structure and strain-relaxation effects of defects in $In_xGa_{1-x}N$ epilayers

S. L. Rhode[1, a*], W. Y. Fu[1, a], M. A. Moram[1, 2], F. C.-P. Massabuau[1], M. J. Kappers[1], C. McAleese[1], F. Oehler[1], C. J. Humphreys[1], R. O. Dusane[3], and S.–L. Sahonta[1]

1) Department of Materials Science and Metallurgy, University of Cambridge, Charles Babbage Road, Cambridge, CB3 0FS, UK

2) Department of Materials, Imperial College London, Exhibition Road, SW7 2AZ, UK

3) Department of Metallurgical Engineering and Materials Science, Indian Institute of Technology Bombay, Mumbai, 400076, India

*sr583@cam.ac.uk

a) S. L. Rhode and W. Y. Fu contributed equally to this work.

Abstract

The formation of trench-defects is observed in 160 nm-thick $In_xGa_{1-x}N$ epilayers with $x \leq 0.20$, grown on GaN on (0001) sapphire substrates using metalorganic vapour phase epitaxy. The trench-defect density increases with increasing indium content, and high resolution transmission electron microscopy shows an identical structure to those observed previously in InGaN quantum wells, comprising meandering stacking mismatch boundaries connected to an I_1-type basal plane stacking fault. These defects do not appear to relieve in-plane compressive strain. Other horizontal sub-interface defects are also observed for these samples and are found to be pre-existing threading dislocations which form half-loops by bending into the basal-plane, and not basal-plane stacking faults, as previously reported by other groups. The origins of these defects are discussed, and are likely to originate from a combination of the small in-plane misorientation of the sapphire substrate and the thermal mismatch strain between the GaN and InGaN layers grown at different temperatures.

Introduction

The direct band gap of $In_xGa_{1-x}N$ can be engineered to emit light over the entire visible spectrum depending on the In content (x) of the film. InGaN-based alloys are thereby used to fabricate light-emitting diodes (LEDs), laser diodes (LDs) [1] [2] and solar cells [3] [4]. InGaN alloys are excellent candidates for the light-absorption layers in solar cell applications because of their high-energy radiation resistance [3] and because InGaN alloys across the

range of In compositions absorb light across the whole solar spectrum in a multi-junction solar cell [5]. While thicker layers of around 100 nm are grown for solar cell applications [6], strained InGaN layers of between 2 and 5 nm are commonly deposited by metalorganic vapour-phase epitaxy (MOVPE) as multiple quantum wells (MQWs) in LED and LD devices. Moreover, 24 to 80 nm thick $In_xGa_{1-x}N$ ($0.03 < x < 0.05$) *underlayers* deposited directly beneath multiple quantum wells in LEDs have been observed to increase LED external quantum efficiencies [6-8].

The growth of relatively thick $In_xGa_{1-x}N$ epilayers on GaN on (0001) sapphire by MOVPE is challenging since the In-N bond is unstable at the high temperatures of around 1000 °C necessary for high-quality GaN growth. Despite a mature growth technology for the deposition of thin $In_xGa_{1-x}N$ QWs by MOVPE, the growth of thick $In_xGa_{1-x}N$ epilayers on GaN remains challenging, resulting in films with high strain and a rich defect microstructure [9].

V-defects appear as V-shaped voids in cross-sectional transmission electron microscopy (TEM) images of $In_xGa_{1-x}N$ films and are the most extensively studied defects in both $In_xGa_{1-x}N$ MQW [10-16] and epilayer [17-19] samples. They are formed when a threading dislocation, usually generated at the interface between the GaN buffer and the substrate [20] propagates along <0001> into the InGaN layer and ultimately opens up as an inverted hexagonal pyramidal pit at the film surface. The six hexagonally-oriented facets of the pit comprise inclined {10-11}-type planes. In the case of MQWs, V-defects tend to originate in the first InGaN quantum well and can permeate through the entire MQW stack depending on the (In)GaN quantum barrier growth condition [21]. Owing to their distinct crater-like shape when viewed using TEM, it was initially suggested that V-defects may be surface terminations of hollow-core screw-type dislocations, first described by Frank [22]. However, since III-nitride films which do not contain indium, (*i.e.* GaN, AlN) do not show pyramidal defects at dislocation cores, a mechanism relating to the growth kinetics was instead proposed. TEM work by Shiojiri *et al.* [21] suggested that during $In_xGa_{1-x}N$ growth, adsorbed indium atoms migrate to the dilatational strain field of dislocation cores to create Cottrell atmospheres [23], resulting in a reduced growth rate directly above the indium-rich dislocation core which leads to the formation of a small pit. At the low temperatures of 700 to 800 °C that are typically used for $In_xGa_{1-x}N$ growth, the growth rate of the flat (0001) surface surrounding the pit tends to be higher than that of the inclined {10-11} surfaces in order to minimise indium adatom desorption, resulting in the pit growing with inclined {10-

11}-type sidewalls to create a hexagonal pyramidal void. This suggests that V-defect formation is kinetically-driven and occurs independently of, yet may be aided by, the presence of impurities such as fluctuations in indium content during low-temperature growth [21].

Furthermore, studies have reported that a V-defect apex may be connected to a stacking mismatch boundary (SMB), which in turn is associated with a stacking fault (SF) within the MQW stack [24-25]. As well as the V-defect, $In_xGa_{1-x}N$ MQW [26-28] and LED structures [29] have been shown to contain high densities of *trench-defects*, which have been shown by atomic force microscopy to consist of trenches with inclined sidewalls which form loops enclosing sections of $In_xGa_{1-x}N$ MQW with different emission properties from the surrounding material [30]. Cross-sectional TEM revealed that these trenches are connected to SMBs, two-dimensional defects oriented along <1-100> and <11-20> in wurtzite materials, which are themselves associated with an I_1-type basal plane stacking fault (BSF) located in the MQW stack [28]. It is possible that the V-defects which were reported to be connected to SMBs and BSFs [24-25] may have been trench-defects which were incorrectly identified as V-defects, owing to their similarity in cross-section. Trench-defects may be distinguished easily from V-defects since the trenches typically appear as two overlapping V-shaped voids when viewed in cross-sectional TEM images, owing to the projection of the trench through the TEM foil. Although trench-defects have been previously observed in thick $In_xGa_{1-x}N$ epilayers [31], their atomic structure has never been studied for such samples.

In addition to trench-defects, some TEM studies suggest that BSFs appear to lie below the InGaN/GaN interface, by as much as 100 nm into the GaN buffer layer [19, 32-33]. The presence of stacking faults below the interface was attributed by Romano *et al.* [32] to the relaxation of high compressive strain which induces shear and therefore slip in the basal-plane [32]. However these features have never been characterised in detail to confirm which type of defect they are, and no mechanisms as to their formation have been proposed in the literature. Hence, in this report, we study the structure of extended defects such as the trench-defects and the horizontal defects below the GaN/InGaN interface in 160 nm-thick InGaN films with varying indium contents. Moreover, previous $In_xGa_{1-x}N$/GaN X-ray diffraction (XRD) studies [32, 34-37] show that high-quality films containing defects such as V-, trench- and horizontal defects are still highly strained even when indium contents and thicknesses are far beyond the critical limit (CL) [38-39] for strain relaxation via plastic deformation. Our

theoretical and experimental results further reveal reasons for the low degree of strain-relaxation present in thick $In_xGa_{1-x}N$ films with x≤0.20.

Experimental Methods

All samples were grown in a Thomas Swan 6 x 2" close-coupled showerhead MOVPE reactor. Trimethylgallium (TMG), trimethylindium (TMI) and ammonia were used as precursors for Ga, In and N, respectively. Silicon doping was achieved using silane as the precursor. Three 160 nm-thick Si-doped ([Si] = 4×10^{18} cm^{-3}) $In_xGa_{1-x}N$ epilayers with varying x (0.05 to 0.20 wt% In) were grown on 3.5 µm-thick low dislocation density (LDD) (threading dislocation density (TDD) of ~4×10^{8} cm^{-2}) GaN epilayers grown on sapphire (0001) substrates. Whilst hydrogen (H_2) was used as a carrier gas for the growth of the GaN templates, nitrogen (N_2) was used as the carrier gas during $In_xGa_{1-x}N$ growth. All samples were grown on sapphire substrates with a miscut angle of 0.25 ± 0.1° along <11-20>$_{sapphire}$ (*i.e.* <1-100>$_{GaN}$). For GaN growth, the sapphire substrate was heated to 1050 ºC in a flow of 3 slm of NH_3 at 1.33 x 10^4 Pa, and annealed for 120 s followed by 180 s of growth with an additional flow of SiH_4 at 200 nmolmin^{-1}. The temperature was then reduced to 540 ºC, the pressure increased to 6.6x10^4 Pa, and a 30 nm GaN NL was grown, which was then annealed at 1010 ºC after growth for 240 s in order to encourage 3D island formation to decrease the TDD. Next, GaN growth was commenced at a lower temperature (980 ºC) for 1200 s, then continued at 980 ºC for 690s, finally followed by 1260 s of growth at 1010 ºC. Further details of GaN epilayer growth on sapphire have been described elsewhere [40-41]. The indium content was varied by keeping the TMI flux constant and reducing the reactor susceptor temperature to incorporate more indium into the epilayer. Previously, WDX, XRD and RBS measurements were performed to investigate the indium wt.% in the samples. WDX measurements predict In wt% of x = 0.057±0.01, 0.128±0.01 and 0.20±0.01 [33]) for the three 160 nm thick $In_xGa_{1-x}N$ epilayer samples labelled as A, B and C, respectively. XRD and RBS studies have predicted only slight variations in the indium content along the growth directions of such layers. For example, values of 0.108-0.122 and 0.121-0.127±0.01 were predicted for sample B when a linear variation along the [0001] is taken into account by XRD and RBS, respectively [31]. Samples A, B and C were grown at temperatures of 750 °C, 725 °C and 710 °C, respectively. In addition to these $In_xGa_{1-x}N$ epilayers, a 110 nm GaN epilayer (D) was also studied to investigate the effect of compressive interfacial strain introduced by In in the $In_xGa_{1-x}N$ layers. Sample D was grown with all reactor conditions

similar to that of A, except that no TMI was introduced during the growth of the low-temperature GaN epilayer. For comparison with sample D, sample E which is an LDD GaN epilayer grown at 1010 °C on sapphire with no subsequent deposition, was also studied during the course of this work.

High-resolution X-ray diffraction was performed in a Philips X' Pert diffractometer using Cu $K\alpha_1$ radiation with a double-bounce Ge (220) asymmetric monochromator and a double-bounce analyser. Reciprocal space maps (RSMs) were recorded for the symmetric 0006 and asymmetric 20-24 reflections to measure *a* and *c* lattice parameters respectively, in order to examine the strain state of the three epilayer samples. The lattice constants were calculated using the method described by Fewster *et al.* [42] applied to our materials [43], assuming Vegard's law as valid (assuming isotropic and linear biaxial strain). The bowing parameter has been shown to be insignificant for the range of x in our samples [44-45]. Finally, values for relaxation (R) in these layers were measured by applying opposite deformations to InGaN layers in order to get an equivalent InGaN lattice on top of relaxed GaN substrates [42].

Atomic force microscopy (AFM) was carried out using a Veeco Dimension 3100 microscope in tapping mode. Cross-sectional and plan-view TEM and high-resolution (HR) TEM were performed using a Philips CM30 (300 kV) and JEOL 4000 EX-II (400 kV) TEM respectively. In addition, plan-view scanning transmission electron microscopy (STEM) using the high-angle annular dark-field (HAADF) detector was performed at 200 kV using the JEOL 2100. Electron-transparent TEM samples were prepared by mechanical polishing, followed by dimpling and back-thinning with Ar^+ ions at 5 kV, and final ion milling at 2 kV to minimize specimen damage.

A three-dimensional dislocation dynamics simulation was performed with the PANIC model [46]. A simulation cell containing 8 pre-existing threading dislocations was set up with randomly-assigned Burgers vector directions (assuming a 1:1 ratio of *a*-type and *(a+c)*-type dislocations in an LDD GaN template [47]). Simulation parameters were set according to Fu *et al*. [46] and experimental growth parameters were set as described earlier, that is, the growth temperatures of the GaN and $In_xGa_{1-x}N$ (x = 0.20) layers were set to 1010 °C and 710 °C respectively.

Results and Discussion

Biaxial Strain

It is well known from previous studies that growth of thick InGaN on GaN buffer layers introduces high biaxial compressive strain at the interface [18, 32, 34-37]. The three $In_xGa_{1-x}N$ films in this report were analysed by XRD in order to measure the residual strain present in the samples after growth.

The RSMs presented in Figure 1 show the 204 reflections of both GaN and InGaN layers. The vertical and inclined dashed lines represent the positions of a fully strained and fully relaxed layer grown on GaN respectively (no significant offset could be seen on the RSMs around the GaN 006 reflection). The small horizontal arrows indicate the lateral misfit strain relaxation in the $In_xGa_{1-x}N$ layer with respect to the GaN buffer layer. Figure 1 shows that this strain relaxation is small for samples B and C and almost negligible for sample A. This indicates that the InGaN layer in sample A is fully strained and those of samples B and C are only partially relaxed. This was confirmed by the values of relaxation (R) which were obtained by applying opposite deformations to the $In_xGa_{1-x}N$ layers, equivalent to InGaN lattices on top of relaxed GaN substrates [42]. The relaxation values calculated were 6 ± 2 % and 8 ± 1 % for B and C respectively, implying that the residual interfacial strain in both the films was around 94 % and 92 %, respectively.

In order to understand the reason for the low degree of strain relaxation, the interfacial regions of films A, B and C were further investigated by HRTEM (not shown) by viewing the sample along the $\langle 11\text{-}20 \rangle$ zone axis and tilting it to excite diffraction conditions **g** = (1-100). The $\vec{a}$-type (b=1/3$\langle 11\text{-}20 \rangle$) [24, 48] misfit dislocations (MDs) are the most commonly observed MDs found in the InGaN/GaN system. They are ideally observed when the sample is tilted near the $\langle 11\text{-}20 \rangle$ zone axis as also observed by Lü *et al.* [48]. The **g**, **0** and **–g** beams were isolated within the objective aperture to observe extra-half planes in 1-100 lattice fringes at the interface. Although randomly-spaced, non-periodic dislocations were visible at the interface, no periodic MDs, an indication of plastic strain-relaxation were observed for all the three $In_xGa_{1-x}N$ ($0.57<x<0.20$) samples. This is in agreement with the study performed on MOVPE-grown InGaN epilayers by Srinivasan *et al.* [49] where a 100 nm thick $In_xGa_{1-x}N$ (x=0.1) layer was also reported to contain randomly-spaced, non-periodic MDs, confirming that their sample as well as our thick $In_xGa_{1-x}N$ ($0.20<x<0.057$) layer samples have all been grown pseudomorphically on GaN with very little strain relaxation. As the field of view of a TEM image is typically a few microns of interface, much larger than the spacings measured

theoretically by our study (198 nm, 59.5 nm and 38.75 nm for sample A, B and C respectively), we further confirm that misfit relaxation has not occurred via the formation of MDs.

Trench-defects

AFM images of the three $In_xGa_{1-x}N$ (0001) surfaces are shown in Figure 2. The dark-spots in all AFM images shown in figure 2 are TD pits whereas the bright arrows indicate trench-defect structures. These images show no change in the V-defects density with an increase in In content from x = 0.057 in sample A to x = 0.12 in sample B. This is further evidence that V-defect formation is not strain-mediated. If V-defect density did increase with In content, then it would be obvious that increased mismatch is creating more V-defects. On the other hand, the trench-defect density increased from $(3 \pm 2) \times 10^5$ cm^{-2} to $(6 \pm 1) \times 10^7$ cm^{-2} when the In content increased from sample A to B. This was confirmed by cross-sectional weak-beam dark-field (WBDF) TEM images for samples A, B and C (figures 4(a), (b) and (c)), where the density of trench-defects increases as the In content in the epilayers is increased. We have tried keeping the imaging conditions for the three images in figure 4(a, b and c) as similar as possible, where the sample was tilted ~3-5° away from the zone-axis to activate the **g** = (1-100) diffraction conditions. This small tilt is not sufficient to remove the electron beam from the plane of the interface as will be shown by the help of STEM-HAADF images in the following section.

Massabuau *et al.* [28] and Sahonta *et al.* [27] both have observed V-pits enclosed by or intersecting the trench-defects in MQW samples, suggesting that the formation of V- and trench-defects are separate phenomena. We already know from literature that V-pit formation is kinetically-driven, but.there is no available evidence that the trench-defect formation is a lattice-mismatch-strain-relaxation-related phenomenon. Moreover, trench-defects do not originate at the InGaN/GaN interface, but ~50-70 nm above the interface in the InGaN layer. This inhibits the trench-defects from relaxing any lattice-mismatch strain at the interface. Low values of strain-relaxation were also measured even when trench-defects were observed in samples B and C and a network of trench-defects was observed in sample C. This is strong evidence that trench-defects do not relieve lattice-mismatch strain at the interface. Nonetheless, these defects may contribute to local strain-relief by the formation of new surfaces, but a high density of such defects would be required for the measurement of any significant strain-relaxation caused by this mechanism.

Trench-defects have been previously extensively studied in $In_xGa_{1-x}N$ MQW structures, and three types of trench-defects were identified according to the relative heights of the trench-enclosed central area with respect to the surrounding material; *lowered-centre* trench-defects have a central MQW region which lies below the surrounding MQW stack, *level-centre* trench-defects have a central enclosure which is at the same height as the surrounding material, and *raised-centre* trench-defects are those where the central region is higher than the surroundings [28].

We find in the case of trench defects in InGaN MQWs that the region within the trench is subject to different growth kinetics from the rest of the film as measured by cathodoluminescence studies [30]. Furthermore, cross-sectioning through a raised-centre trench by Sahonta *et al.* [27] showed that the trench-enclosed region has thicker QWs than the surrounding QW region, suggesting that the QWs grow faster at the defect, and therefore that indium incorporation rate at the defect is higher than at the undefective region during MQW growth. It follows that for a level-centre trench, the growth rate of the InGaN layers in a defective MQW is not affected, and that in lower-centre trenches the growth rate of the MQW region is slower at the defect than in the rest of the film.

It is therefore expected that in the case of $In_xGa_{1-x}N$ ($x \leq 0.20$) epilayers, once a trench defect has formed, the growth rate of material being deposited in the trench-enclosed area will differ from that of the surrounding growth, just as it does for InGaN MQWs. The AFM images (figure 2(a), (b) and (d)) show that the samples A and B with relatively low indium contents of ~6 % and ~13 % have only level-centre (dashed white arrow) or lower-centre trenches (white arrows), suggesting that the InGaN growth rate of the trench-enclosed area has been unaffected or slightly impeded by the presence of the defect, perhaps due to the slower growth rate on the inclined {1-101} face relative to (0001) [56]. On the other hand, sample C with an In content of around 20 % was grown at a much low temperature (710 °C) to incorporate higher indium into the film. We observe mostly raised-centre trenches for this sample as indicated by black arrows in figure 2(e). This suggests that the local growth rate increases within the trench-enclosed area, perhaps due to the relative relaxation of the lattice in the trench-enclosed area with respect to the rest of the film. If the region within the trench-defect is a region of lattice relaxation, it will be easier to incorporate the larger In atoms into the lattice at that point, resulting in a higher local growth rate at the defect forming raised-centre trench-defects.

The atomic structure of a trench-defect was further studied by acquiring HRTEM images along the <11-20> zone axis, where the trenches themselves appeared to be connected to an I_1-type BSF *via* planar SMBs, as seen in figure 4(a),. The stacking sequence of atomic columns was labelled in figure 4(b), which is a higher magnification image of the black dotted box identified in Fig. 4(a), to observe the atomic structure of the defect. It clearly shows an SMB where the wurtzite bB atomic stacking changes to cC stacking at the interface of the SMB with the surrounding InGaN. As there is one single violation of the stacking rule in the planar fault at the bottom of the SMB along the *c*-axis (stacking sequence of aAcCaA**cCaAbB**aAbB exists at the fault instead of aAcCaAcCaAcCaAcC stacking observed for an ideal hexagonal lattice), the fault was identified as an I_1 BSF. Thus, this HRTEM study on sample C reveals that the structure of trench-defects in $In_xGa_{1-x}N$ ($x \leq 0.20$) epilayers is identical to that reported for trench-defects in MQW structures [28].

Further TEM studies were performed to identify the crystallographic orientation of these defects. As trench-defects were studied in detail by Massabuau *et al.* [28] for InGaN/GaN MQW samples, we aim to identify the differences in the defect structure between the InGaN MQW and thick epilayer samples. Previous studies on InGaN MQW samples have suggested that the temperature and hydrogen environment during QW GaN barrier growth plays a vital role in trench-defect formation [26, 57-58]. As growth parameters and conditions are considerably different for thick InGaN epilayers as compared to the InGaN MQW samples, it is worth studying the structure of trench-defects in our samples. The motivation is to ultimately identify factors which contribute to and affect their formations.

Figure 5 shows an image of a trench-defect in sample B (and a nearby V-defect indicated by a hexagon) taken along the [0001] direction of the sample using the STEM-HAADF imaging mode of the microscope. It is well established in literature that the {1-101}-faceted V-pit edges run along the <11-20> directions [11, 59]. Taking this as a reference, the directions of the SMBs delineating the boundaries of the trench-defects were established as both <11-20> and <1-100>, with more sections of trenches lying along <11-20>. This agrees with studies on trench-defects in MQW samples and is expected since the SMBs are generated most easily along the close-packed <11-20> directions. Moreover, it is relatively more energetically-favourable for an SMB to change its direction along the close-packed <11-20> axis compared to <1-100>. Thus, SMBs travelling parallel to <1-100> appear straight as seen in figure 5. Moreover, every time the SMB changes its direction along the <11-20> directions, an additional pit is generated. This can also be seen in figure 2(d) where dark lines delineating

trench-defects are formed by the merging of small pits formed each time the SMB changes its direction along the <11-20>, as also observed previously by Massabuau *et al.* [28] and further demonstrated by a schematic of a trench-defect shown in figure 6(a).
In addition to trench-defects, figures 2(c) and (e) show large features of ~650 nm diameter (inside boxed areas), accompanied by an increase in the RMS roughness value from 1.2214 nm measured at a trench-defect in B to 3.6859 ± 0.5 nm measured at the large feature in C seen in using the Nanotec Electronica WSxM software to process AFM images [60] (2(d and e)).
We have already attributed the formation of raised-trenches in the low-temperature grown sample C to the higher growth rates inside the trenches as compared to the surrounding material.

Sub-Interfacial Extended Defects

In addition to V-defects and trench-defects, extended defects have been observed lying in the basal plane below the InGaN/GaN interface [19, 32-33, 49]. These defects have previously been described as BSFs although no defect analysis has been performed, and it has been proposed that their origin relates to the compressive strain in the InGaN layer inducing shear in the less compliant GaN layer [32]. Zhang *et al.* [61] concluded from diffraction contrast imaging from different orientations that they are horizontal line defects rather than stacking faults. If we consider this extended defect to be an I_1 BSF as suggested in some reports [19, 32-33], it should only be visible for the **g** = (1-100) diffraction condition based on the g.R criterion [62-63]. The g.R criteria is valid for such strained thick $In_xGa_{1-x}N$ ($x \leq 0.20$) epilayers as also shown in work by Meng *et al.* [63] where x was 0.07 and in work by Srinivasan *et al.* [49] where x was 0.10. Moreover, SFs in thick epilayers similar in composition and thickness to our samples (100 nm thick $In_xGa_{1-x}N$ epilayers with x=0.07) were only observed for the **g** = (1-100) diffraction condition [63], confirming that the g.R criteria valid for stacking-faults [62] is valid for our samples A, B and C as well. On the contrary, cross-sectional WBDF TEM images for sample C (figure 8), as well as defect studies reported by Romano *et al.* [32] show these defects as visible under the **g** = (11-20) diffraction condition, confirming that such defects are not BSFs.

Our calculations using the PANIC model (considering climb and also glide in all possible slip systems in a wurtzite crystal), which simulate the early stages of epilayer growth, further suggest that these sub-interface horizontal defects are actually bowed-out TDs. This bow-out

of TDs results in two horizontal segments with opposite line directions but the same Burgers vector, as shown in the simulated dislocation microstructure in figure 9(a). Therefore, very little strain can be relaxed by this type of defect as their strain fields are oriented parallel to each other in the film.

While figure 9(b) shows a STEM-HAADF image showing a half-loop containing the two horizontal segments (separated from each other by 3 to 15 nm) with opposite line directions, figure 10(c) shows a schematic of TD segments bowing-out from an existing TD. Although these sub-horizontal segments were observed in figure 3(b, c) where the sample was tilted to activate WBDF activating the **g** = (1-100) diffraction conditions, the tilt was ~3-5 ° and thus very close to the <11-20> zone axis. This small tilt is not sufficient to remove the electron beam from the plane of the interface as a STEM-HAADF image taken along the <11-20> zone-axis for sample C (figure 9(b)) shows the same sub-interfacial defects as observed in the WBDF images shown in figure 3(b and c). This is also supported by the observation of sub-interfacial defects in a STEM-HAADF image taken along the zone-axis on a 200 nm thick $In_xGa_{1-x}N$ (x=0.12) epilayer at similar distances in the GaN substrate below the InGaN/GaN interface [61] when compared with the STEM-HAADF image (figure 9(b)) and WBDF images (figure 3) of sample C. The STEM-HAADF image was intentionally taken on the zone-axis in order to compare well with the simulation in figure 9(a). As the activation energy for dislocation motion in GaN is relatively small [64], TDs can bow out for several micrometers as shown in the STEM-HAADF image of sample C in figure 3(b), making it difficult to observe half-loops using TEM even when a high density of horizontal TDs (top and bottom edges of the loop) are observed below the $In_xGa_{1-x}N$/GaN interface, as seen in both figures 3(b) and 3(c). Thus, several TEM samples were prepared to acquire a single image of a TD loop.

The figure 10(c) is shown to confirm that a TD bows out to form a long loop, and the edges of the loop are indeed the horizontal sub-interfacial defects observed for the InGaN/GaN epilayer system. Thus, it is established experimentally by TEM and theoretically by the PANIC dislocation dynamics model that these sub-interface defects are TDs that bend below the $In_xGa_{1-x}N$ /GaN interface.

Furthermore, our energy-balance critical-thickness calculations [65] (considering glide on the 1/3 <11-23> {1-101} slip system) predict that this bowing has taken place well before the $In_xGa_{1-x}N$ layer reached its theoretical CT [38-39]. This is shown in figure 11 where our

calculations imply that the compressive thermal mismatch introduced by low temperature growth of $In_xGa_{1-x}N$ epilayers introduces biaxial stress on the GaN buffer layer grown at 1010 °C. The thermal mismatch due to different growth temperatures for GaN and $In_xGa_{1-x}N$, together with the small miscut of 0.25 ° ± 0.1 ° of the (0001) sapphire substrate are possible driving forces for the activation of a secondary slip system, 1/3 <11-23> {1-101}, in the GaN template. This is indicated by a dashed line in figure 11 which suggests that the equivalent CT for the onset of glide in the GaN template is above 200 nm, which is far below the thickness of a usual GaN buffer layer (around 3.5 μm for sample C). Glide on the secondary slip systems has also been reported in earlier reports [49] for similar $In_xGa_{1-x}N$ epilayer films.
In order to confirm that the formation of these glissile dislocations is due to thermal mismatch between GaN and InGaN and not an effect of In incorporation, we analysed sample D which is a 110 nm-thick GaN epilayer grown at a temperature typical for InGaN growth on a standard LDD GaN buffer on 0.25 ° ± 0.1 °-miscut (0001) sapphire, and sample E which is the GaN buffer layer only, grown at 1010 °C on 0.25 ° ± 0.1 °-miscut (0001) sapphire. It is certain that no compressive strain due to lattice mismatch exists for sample D as the epilayer does not contain any indium, although thermal mismatch stresses will be present due to differences in growth temperatures. However, WBDF **g**(2**g**) TEM images for sample D activating **g** = (1-100) diffraction conditions also show sub-interface TDs lying in the basal-plane as observed in figure 11(a). Simulations also confirm that these defects are bowed-out TDs (figure 11(b)) as seen previously below the GaN/$In_xGa_{1-x}N$ interfaces (figure 9). Moreover, as no sub-interface dislocations were observed for sample E [47], it can be confirmed that the observed bowed-out TDs and half-loops only appear when subsequent epilayers are grown at comparatively low temperatures.
Dislocation simulation studies were reported only at one composition (sample C) as glide on the 1/3 <11-23> {1-101} slip system is an effect of thermal-mismatch between the InGaN and GaN films. Sample C has the highest thermal-mismatch as the underlying GaN template was grown at 1010 °C as compared to growth temperatures of 750 °C, 725 °C and 710 °C for sample A, B and C, respectively. Hence, more TDs glide on the secondary slip system forming loops in sample C. This increases the probability of observing dislocation loops both in a TEM foil and a simulation cell. Thus, sample C was the ideal choice to compare a TEM image with its simulated dislocation microstructure, with regards to studying sub-interfacial defects in the InGaN/GaN system.

These results imply that thermal mismatch stresses play a major role in the development of the observed dislocation microstructure in both (thick) $In_xGa_{1-x}N$ ($x \leq 0.20$) and GaN epilayers grown at relatively low temperatures.

Discussion

Our XRD studies, in addition to previous studies, establish that $In_xGa_{1-x}N$ ($x \leq 0.20$) films grow pseudormorphically on GaN pseudo-substrates, even when indium contents and thicknesses are far beyond the critical limits for plastic relaxation by the generation of MDs at the $In_xGa_{1-x}N$/GaN interface. In addition, our TEM studies show that these films do not contain repetitive MDs that relieve strain at the $In_xGa_{1-x}N$/GaN interface. Although strain is expected to remain in wurtzite (0001) films after growth, owing to the fact that there is no resolved shear force on the basal-plane which inhibits strain relief *via* dislocation glide on the main slip system in hexagonal materials ({0001} <11-20>), biaxial strain may perhaps be relieved by the presence of other extended defects in the film which may reduce misfit strain below the critical value for MD formation. For example, V-defects which provide a local increase in the film surface area, should relieve some amount of strain [18, 49]. However, extremely high densities of such defects are necessary for any measurable relaxation to be observed by XRD [67]. Moreover, as the V-defect density in this work is relatively low ($4 \pm 0.3 \times 10^{-8}$ cm^{-2}), it is unlikely that V-pits completely relieve mismatch strain as also suggested by Song *et al.* [18]. This is also the case for trench-defects and TDNs, where the relief of interfacial strain by local increases in film surface area inside the trench [30] only accounts for strain reduction of a few *per cent*. The fact that the films are highly strained is surprising however, since despite there being no mechanism for dislocation glide in the {0001} <11-20> slip system to relieve interfacial strain, TDs in nitride materials may *climb* into the basal-plane, thus forming periodic misfit segments at the interface as also seen by Sahonta *et al.* [68]. Although this TD motion is possible [69], it has not occurred in these films, perhaps owing to the low equilibrium concentrations and self-diffusion constants of vacancy defects in GaN [70]. Instead, slip on a secondary slip system below the InGaN/GaN interface was observed by our simulations using the PANIC model. This mechanism forms half-loops containing two horizontal segments of opposite line direction which cancel each other's energies and thus limit any strain relaxation caused by the presence of horizontal defects in such $In_xGa_{1-x}N$ epilayers. This explains the presence of high residual strain in thick $In_xGa_{1-x}N$ samples despite their rich defect microstructure.

Conclusions

Trench-defects in InGaN epilayer samples have been studied in detail and their structure was found to be identical to those observed in InGaN QWs [4], comprising meandering stacking mismatch boundaries (SMBs) connected to a type I_1 BSF. Furthermore, trench-defects appear to evolve into more complex TDN structures as the indium content of the film increases. Moreover, sub-interface horizontal defects were investigated experimentally by TEM and theoretically by the PANIC dislocation dynamics model. Results show that these defects are not BSFs as reported previously, but pre-existing threading dislocations, generated originally at the GaN/sapphire interface, which bend into the *c*-plane forming half-loops as a result of thermal mismatch strain (as the epilayers were grown at lower temperatures than the GaN buffer layer), and from the miscut of the sapphire (0001) surface (0.25 ° ± 0.1 ° along <11-20>) which allows TDs to glide on the secondary slip system of $^1/_3$ <11-23> {1-101}. These results provide a useful insight into the structure and formation mechanisms of different defects found in 160 nm-thick technologically relevant $In_xGa_{1-x}N$ epilayers with $x \leq 0.20$ grown on GaN.

Acknowledgements

This work was funded in part by the Cambridge Commonwealth trust and the EPSRC. SKR is funded through the Cambridge-India Partnership Fund and Indian Institute of Technology Bombay via a scholarship. SKR also acknowledges funds from St. John's College. MAM acknowledges support from the Royal Society through a University Research Fellowship.

References

[1] S. Nakamura, T. Mukai, M. Senoh, Appl. Phys. Lett., **64**, 1687, 1994.

[2] F. A. Ponce and D. P. Bour, Nature, **386**, 351, 1997.

[3] J. Wu, W. Walukiewicz, K. M. Yu, W. Shan, J. W. Ager III, E. E. Haller, H. Lu, W. J. Schaff, W. K. Metzger, S. Kurtz, J. Appl. Phys., **94**, 6477, 2003.

[4] O. Jani, I. Ferguson, C. Honsberg, S. Kurtz, Appl. Phys. Lett., **91**, 132117, 2007.

[5] R. Singh, D. Doppalapudi, T. Moustakas, L. Romano, Appl. Phys. Lett., **70**, 1089, 1997.

[6] T. Li, Q. Y. Wei, A. M. Fischer, J. Y. Huang, Y. U. Huang, F. A. Ponce, J. P. Liu, Z. Lochner, J.-H. Ryou, R. D. Dupuis, Appl. Phys. Lett., **102**, 041115, 2013.

[7] T. Akasaka, H. Gotoh, T. Saito, T. Makimoto, Appl. Phys. Lett., **85**, 3089, 2004.

[8] M. J. Davies, F. C. -P. Massabuau, P. Dawson, R. A. Oliver, M. J. Kappers and C. J. Humphreys, Phys. Stat. Solidi C, **11**, 710, 2014.
[9] S. Mahajan, Scripta Materialia, **75**, 1, 2014.
[10] X. H. Wu, C. R. Elsass, A. Abare, M. Mack, S. Keller, P. M. Petroff, S. P. DenBaars, J. S. Speck, S. J. Rosner, Appl. Phys. Lett., **72**, 692, 1998.
[11] Y. Chen, T. Takeuchi, H. Amano, I. Akasaki, N. Yamada, Y. Kaneko, S.Y. Wang, Appl. Phys. Lett., **72**, 710, 1998.
[12] N. Sharma, P. Thomas, D. Tricker, C. J. Humphreys, Appl. Phys. Lett., **77**, 1274, 2000.
[13] F. Scholz, A. Sohmer, J. Off, V. Syganow, A. Dörnen, J. -S. Im, A. Hangleiter, H. Lakner, Mat. Sci. and Technol. B**50**, 238, 1997.
[14] C. J. Sun, M. Zubair Anwar, Q. Chen, J. W. Yang, M. Asif Khan, M. S. Shur, A. D. Bykhovski, Z. Lilliental-Weber, C. Kisielowski, M. Smith, J. Y. Lin, H. X. Jiang, Appl. Phys. Lett., **70**, 2978, 1997.
[15] S. Mahanty, M. Hao, T. Sugahara, R. S. Q. Fareed, Y. Morishima, Y. Naoi, T. Wang, S. Sakai, Mater. Lett., **41**, 67, 1999.
[16] N. Sharma, D. Tricker, P. Thomas, Z. Bougrioua, K. Jacobs, J. Cheyns, I. Moerman, T. Thrush, L. Considine, A. Boyd, C. J. Humphreys, J. Cryst. Growth, **230**, 438, 2001.
[17] I. -H. Kim, H. -S. Park, Y. -J. Park, T. Kim, Appl. Phys. Lett., **73**, 1634, 1998.
[18] T. L. Song, J. Appl. Phys., **98**, 084906, 2005.
[19] H. K. Cho, J. Y. Lee, K. S. Kim, G. M. Yang, J. Cryst. Growth, **220**, 197, 2000.
[20] M. A. Moram, C. S. Ghedia, D. V. S. Rao, J. S. Barnard, Y. Zhang, M. J. Kappers, and C. J. Humphreys, J. Appl. Phys. 106, 073513, 2009.
[21] M. Shiojiri, C. C. Chuo, J. T. Hsu, J. R. Yang and H. Saijo, J. Appl. Phys., **99,** 073505, 2006.
[22] F. C. Frank, *Acta* Cryst., **4**, 497, 1951.
[23] A. H. Cottrell, Proc. Phys. Soc., **62**, 49, 1949.
[24] H. K. Cho, J. Y. Lee, G. M. Yang, C. S. Kim, Appl. Phys. Lett., **79**, 215, 2001.
[25] H. K. Cho, J. Y. Lee, C. S. Kim, G. M. Yang, N. Sharma, C. J. Humphreys, J. Cryst. Growth, **231**, 466, 2001.
[26] S. M. Ting, J. C. Ramer, D. I. Florescu, V. N. Merai, B. E. Albert, A. Parekh, D. S. Lee, D. Lu, D. V. Christini, L. Liu, E. A. Armour, J. Appl. Phys. **94**, 1461, 2003.
[27] S. -L. Sahonta, M. J. Kappers, D. Zhu, T. J. Puchtler, T. Zhu, S. E. Bennett, C. J. Humphreys, R. A. Oliver, Phys. Status Solidi A, **210**, 195, 2013.

[28] F. C.-P. Massabuau, S. -L. Sahonta, L. Trinh-Xuan, S. Rhode, T. J. Puchtler, M. J. Kappers, C. J. Humphreys and R. A. Oliver, Appl. Phys. Lett., **101**, 212107, 2012.
[29] F. C-P. Massabuau, M. J. Davies, F. Oehler, S. K. Pamenter, E. J. Thrush, M. J. Kappers, A. Kovács, T. Williams, M. A. Hopkins, C. J. Humphreys, P. Dawson, R. E. Dunin-Borkowski, J. Etheridge, D. W. E. Allsopp and R.A. Oliver, to be submitted.
[30] F. C.-P. Massabuau, L. Trinh-Xuan, D. Lodié, E. J. Thrush, D. Zhu, F. Oehler, T. Zhu, M. J. Kappers, C. J. Humphreys, R. A. Oliver, J. Appl. Phys, **113**, 073505, 2013.
[31] E. Taylor, F. Fang, F. Oehler, P. R. Edwards, M. J. Kappers, K. Lorenz, E. Alves, C. McAleese, C. J. Humphreys, R. W. Martin, Semicond. Sci. Technol., **28**, 065011, 2013.
[32] L. T. Romano, B. S. Krusor, M. D. McCluskey, D. P. Bour, K. Nauka, Appl. Phys. Lett., **73**, 1757, 1998.
[33] H. K. Cho, G. M. Yang, J. Cryst. Growth, **243**, 124, 2002.
[34] T. Böttcher, S. Einfeldt, V. Kirchner, S. Figge, H. Heinke, D. Hommel, H. Selke, P. L. Ryder, Appl. Phys. Lett., **73**, 3232, 1998.
[35] L. Görgens, O. Ambacher, M. Stutzmann, C. Miskys, F. Scholz, J. Off, Appl. Phys. Lett., **76**, 577, 2000.
[36] M. D. McCluskey, C. G. Van de Walle, L. T. Romano, B. S. Krusor, N. M. Johnson, Appl. Phys. Lett., **93**, 4340, 2003.
[37] F. A. Ponce, S. Srinivasan, A. Bell, L. Geng, R. Liu, M. Stevens, J. Cai, H. Omiya, H. Marui, S. Tanaka, Phys. Stat. Sol. B, **240**, 273, 2003.
[38] C. A. Parker, J. C. Roberts, S. M. Bedair, M. J. Reed, S. X. Liu, N. A. El-Masry, L. H. Robins, Appl. Phys. Lett., **75**, 2566, 1999.
[39] D. Holec, P. M. F. J. Costa, M. J. Kappers, C. J. Humphreys, J. Cryst. Growth, **303**, 314, 2007.
[40] S. Das Bakshi, J. Sumner, M. J. Kappers, R. A. Oliver, J. Cryst. Growth, **311**, 232, 2009.
[41] M. J. Kappers, R. Datta, R.A. Oliver, F. D. G. Rayment, M. E. Vickers, C. J. Humphreys, J. Cryst. Growth, **300**, 70, 2007.
[42] P. F. Fewster and N. L. Andrew, J. Appl. Phys., **74**, 3121, 1993.
[43] F. Oehler, M. E. Vickers, M. J. Kappers, C. J. Humphreys, R. A. Oliver, Jap. J. Appl. Phys., **52,** 08JB29, 2013.
[44] K. P. O'Donnell, I. Fernandez-Torrente, P. R. Edwards, R. W. Martin, J. Cryst. Growth, **269**, 100, 2004.

[45] S. Pereira, M. R. Correia, T. Monteiro, E. Pereira, M. R. Soares, E. Alves, J. Cryst. Growth, **230**, 448, 2001.

[46] W. Y. Fu, C. J. Humphreys, M. A. Moram, J. Mater. Phys. Solids, submitted.

[47] S. K. Rhode, M. K. Horton, M. J. Kappers, S. Zhang, C. J. Humphreys, R.O. Dusane, S.-L. Sahonta, M. A. Moram, Phys. Rev. Lett., **111**, 025502, 2013.

[48] W. Lü, D. B. Li, C. R. Li, F. Shen, Z. Zhang, J. Appl. Phys., 95, 2004.

[49] S. Srinivasan, L. Geng, R. Liu, F. A. Ponce, Y. Narukawa, S. Tanaka, Appl. Phys. Lett., **83**, 5187, 2003.

[50] .T. Romano, B.S. Krusor, R.J. Molnar, Appl. Phys. Lett., 71, 2283, 1997.

[51] C. Stampfl and C. G. Van de Walle, Phys. Rev. B, 57, 15052, 1998.

[52] S. Suandon, S. Sanorpim, K. Yoodee, K, Onabe, Thin Solid Films, 515, 4393, 2007.

[53] J. Kioseoglou, H. M. Polatoglou, L. Lymperakis, G. Nouet, Ph. Komninou,, Comp. Mat. Sci., 27, 43, 2003.

[54] J. E. Northrup, J. Neugebauer, L. T. Romano, Phys. Rev. Lett., 77, 103, 1996.

[55] B. N. Sverdlov, G. A. Martin, H. Morkoç, D. J. Smith, Appl. Phys. Lett., 67, 2063, 1995.

[56] Z. Liliental-Weber, Y. Chen, S. Ruvimov, J. Washburn, Phys. Rev. Lett., 79, 2835, 1997.

[57] M. Senthil Kumar, Y. S. Lee, J. Y. Park, S. J. Chung, C.-H Hong, E.-K. Suh, Mat. Chem. and Phys., 113, 192, 2009.

[58] D. I. Florescu, S. M. Ting, J. C. Ramer, D. S. Lee, V. N. Merai, A. Parekh, D. Lu, E. A. Armour, L. Chernyak, Appl. Phys. Lett., 83, 33, 2003.

[58] Th. Kehagias, G. P. Dimitrakopulous, J. Kioseoglou, H. Kirmse, C. Giesen, M. Heuken, A. Georgakilas, W. Neumann, Th. Karakostas, Ph. Komninou, Appl. Phys. Lett., 95, 071905, 2009.

[59] I. Horcas, R. Fernandez, J.M. Gomez-Rodriguez, J. Colchero, J. Gomez-Herrero and A. M. Baro, Rev. Sci. Instrum. 78, 013705 (2007), www.nanotec.es.

[61] Y. Zhang, M. J. Kappers, D. Zhu, F. Oehler, F. Gao, C. J. Humphreys, Solar Energy Mat. and Solar Cells, **117**, 279, 2013.

[62] F. Y. Meng, M. Rao, N. Newman, R. Carpenter, S. Mahajan, Acta Mater., **56**, 4036, 2008.

[63] F. Y. Meng, H. McFelea, R. Datta, U. Chowdhury, C. Werkhoven, C. Arena, S. Mahajan, J. Appl. Phys., 110, 073503, 2011.

[64] I. Yonenaga, Y. Ohno, T. Taishi, Y. Tokumoto, Physica B, **404**, 4999, 2009.

[65] W. Y. Fu, C. J. Humphreys, M. A. Moram, to be submitted.

[66] S. Pereira, M. R. Correia, E. Pereira, C. Trager-Cowan, F. Swaaney, K. P. O'Donnell, E. Alves, N. Franco, A. D. Sequeira, Appl. Phys. Lett., **81**, 1207, 2002.

[67] D. D. Perovic and D. C. Houghton, Inst. Phys. Conf. Ser., **146**, 117, 1995.

[68] S. -L. Sahonta, M. Q. Baines, D. Cherns, H. Amano, F. A. Ponce, Phys. Stat. Sol. B, **234**, 952, 2002.

[69] M. A. Moram, T. C. Sadler, M. Häberlen, M. J. Kappers and C. J. Humphreys, Appl. Phys. Lett. **97**, 261907, 2010.

[70] L. Sugiura, J. Appl. Phys. **81**, 1633, 1997.

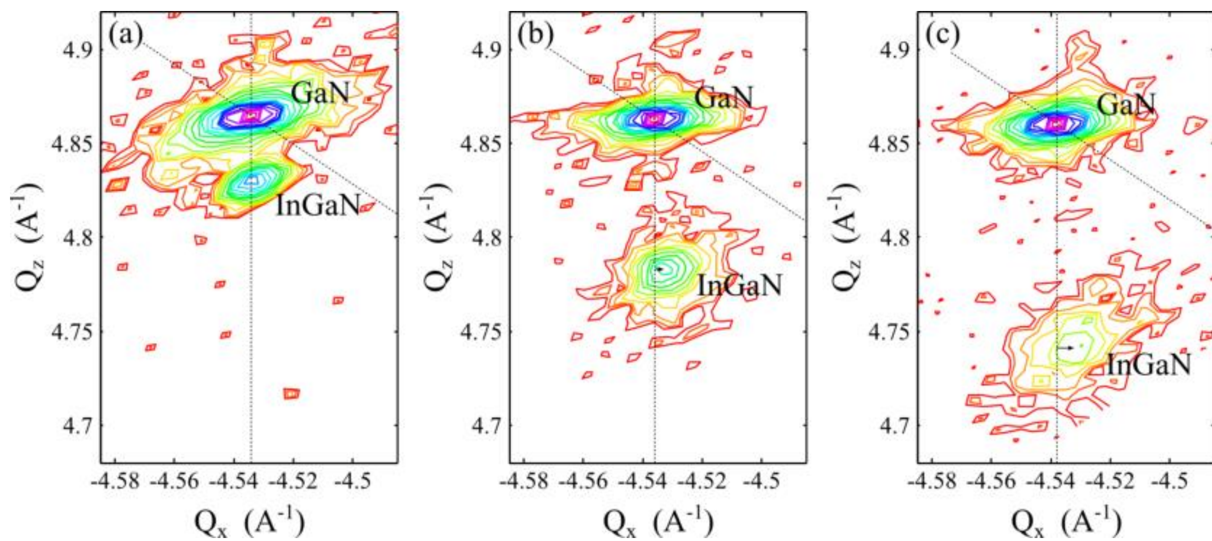

Figure 1: RSMs around the 204 reflections of samples (a) A (b) B and (c) C. The arrows show slight increase in compressive strain relaxation as the InN fraction increases in the samples. Q_x and Q_z are reciprocal lattice spacings and they represent lateral and vertical misfit, respectively.

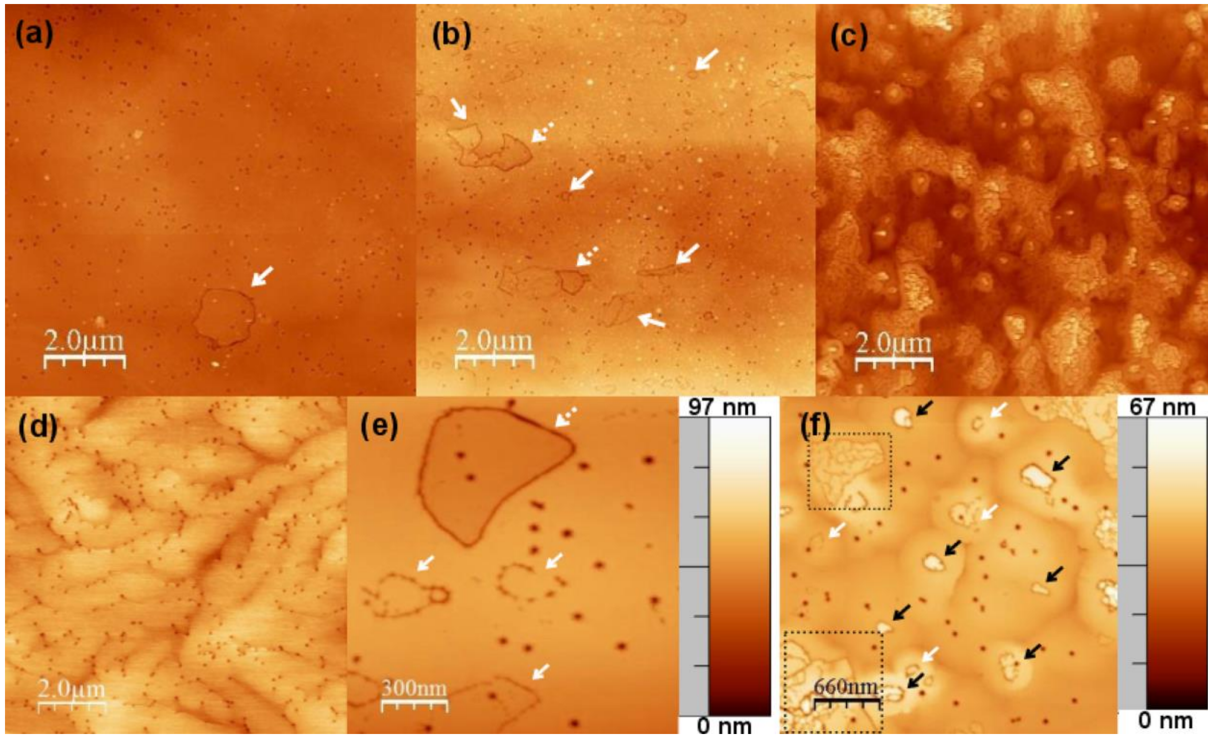

Figure 2: AFM scans of (a) film A, (b) film B (c) film C, (d) film D, (e) high-resolution scan of film B, and (f) high-resolution scan of film C. The arrows indicate trench defect structures and boxed regions indicate TDN structures.

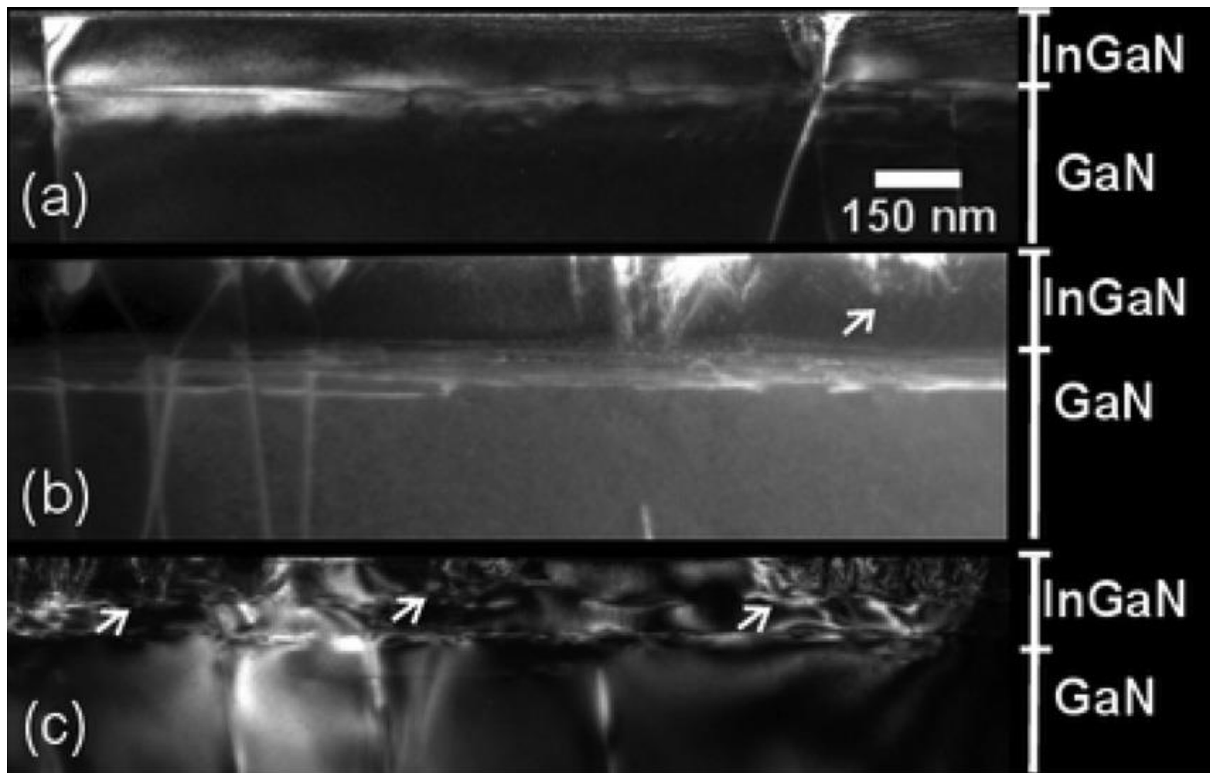

Figure 3: Cross-sectional WBDF TEM micrographs taken under **g**(2**g**) conditions to activate **g** = (1-100) for samples (a) A (b) B and (c) C. The arrows indicate trench-defects in (b) and (c).

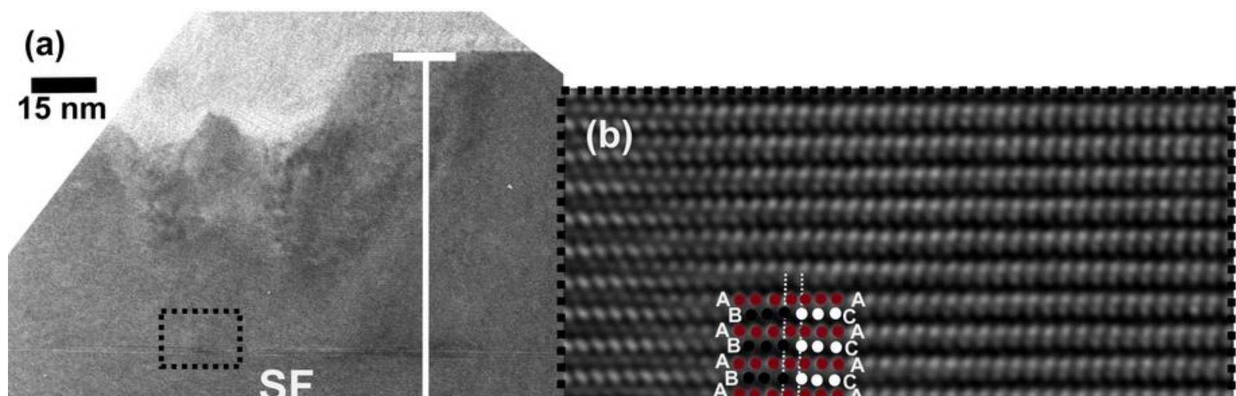

Figure 4: Cross-sectional HRTEM images of sample C along the <11-20> zone axis showing (a) a trench-defect at the InGaN film surface connected to a BSF in the film, (b) magnified image of the black dotted box lying below a trench in (a), showing an SMB connected to an I_1 type BSF.

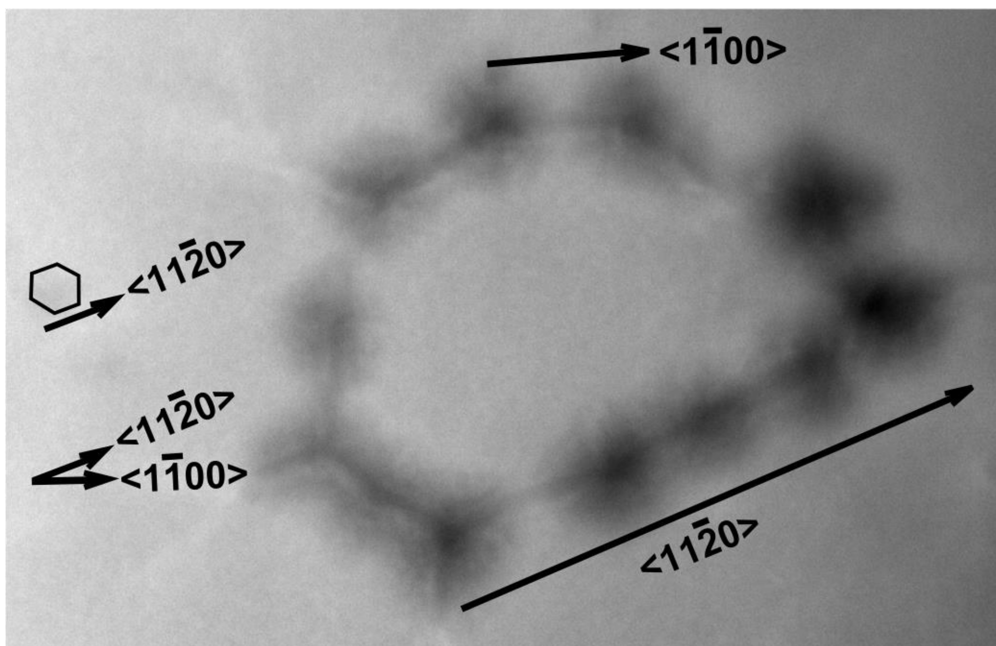

Figure 5: Plan-view STEM-HAADF image of sample B taken along the [0001] zone-axis, showing trench-defect boundary directions along <11-20> and <1-100> with reference to a hexagonal V-pit ending with boundaries along <11-20>.

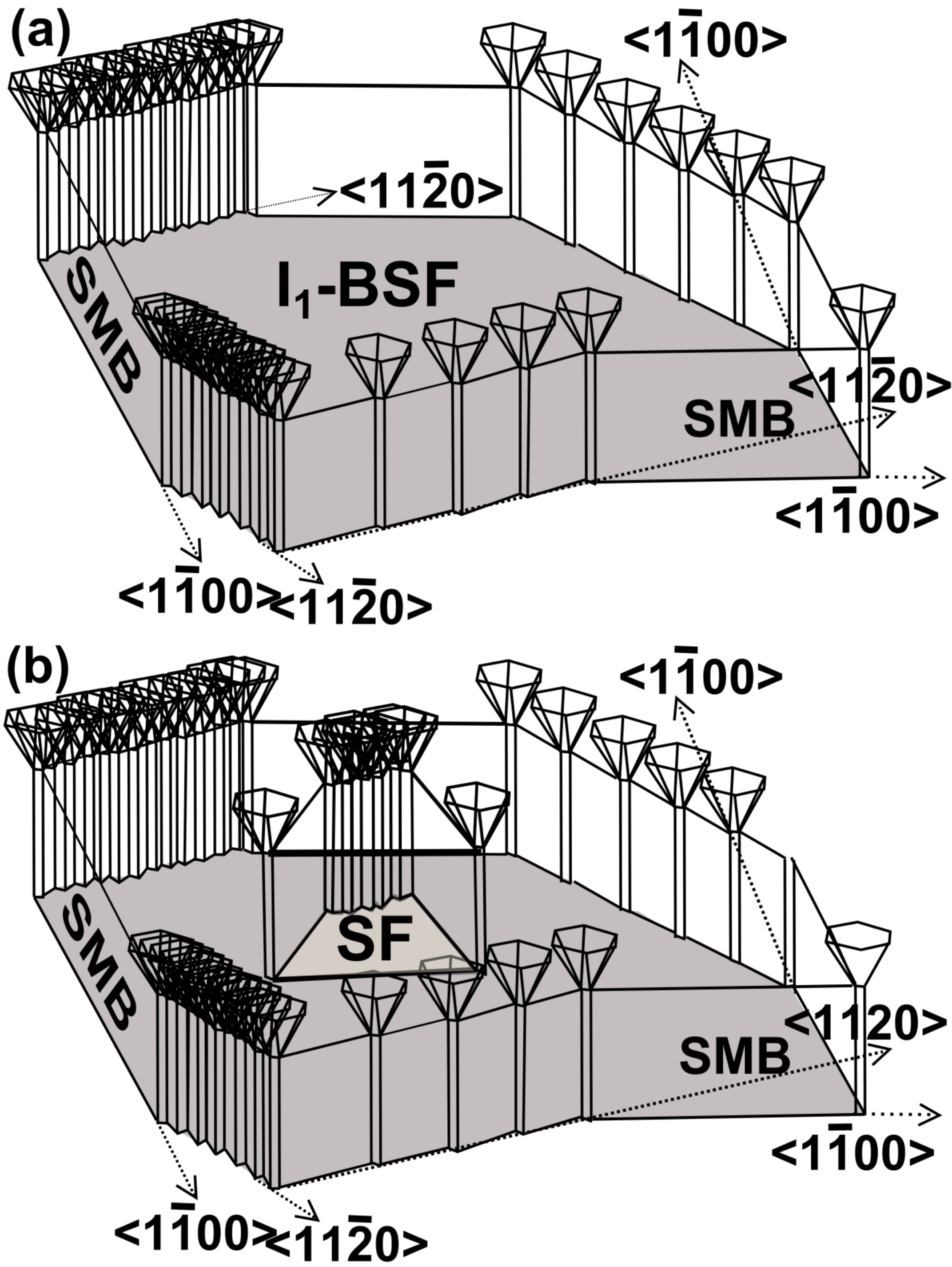

Figure 6: Schematic of a (a) trench and (b) TDN found in thick $In_xGa_{1-x}N$ epilayer samples where a pit is formed every time the SMB changes its direction in the <11-20> direction.

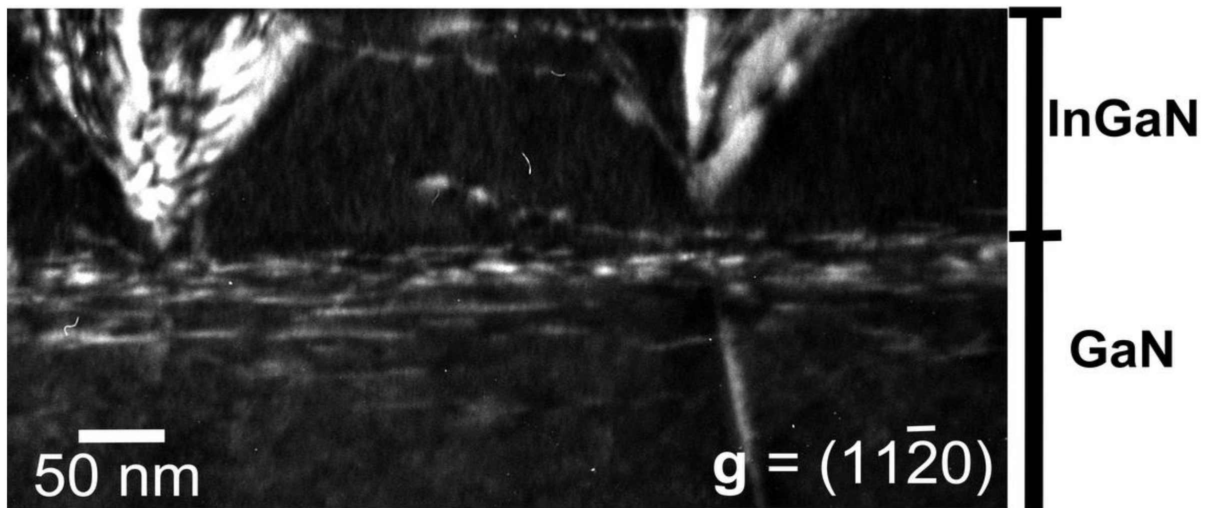

Figure 7: Cross-sectional WBDF **g**(2**g**) TEM image of sample C taken along the <10-10> zone axis and tilted 6 ° to excite the **g** = (11-20) diffraction condition, showing defects below the $In_xGa_{1-x}N$/GaN interface lying parallel to (0001).

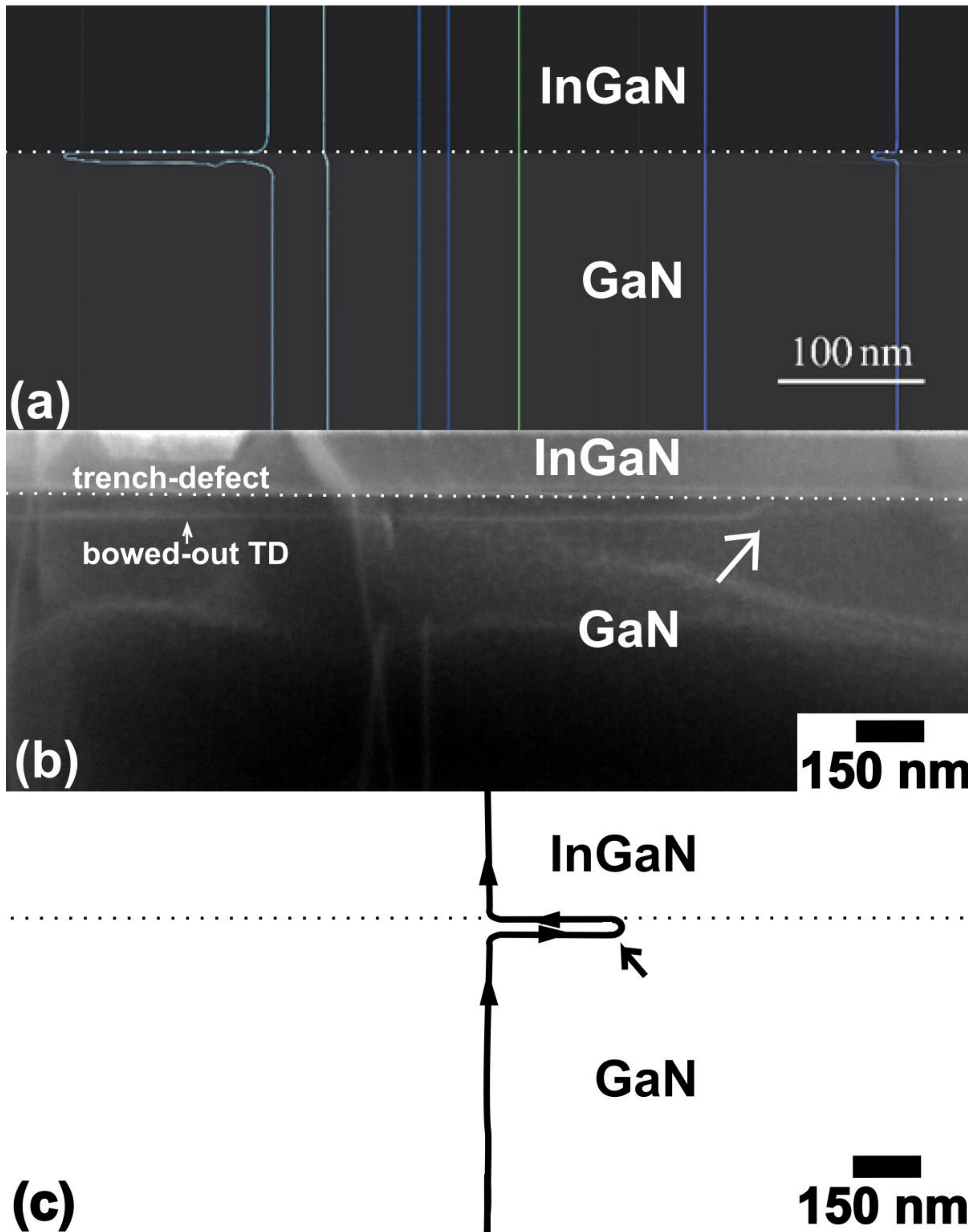

Figure 8: (a) Figure 10: (a) Simulated dislocation microstructure using the PANIC dislocation dynamics model, correlating well with a (b) STEM-HAADF image of sample C taken along the <11-20> zone-axis showing a dislocation half-loop and (c) a schematic of a bending TD below the $In_xGa_{1-x}N$/GaN interface. The dislocation loop is indicated by an arrow in both (b) and (c).

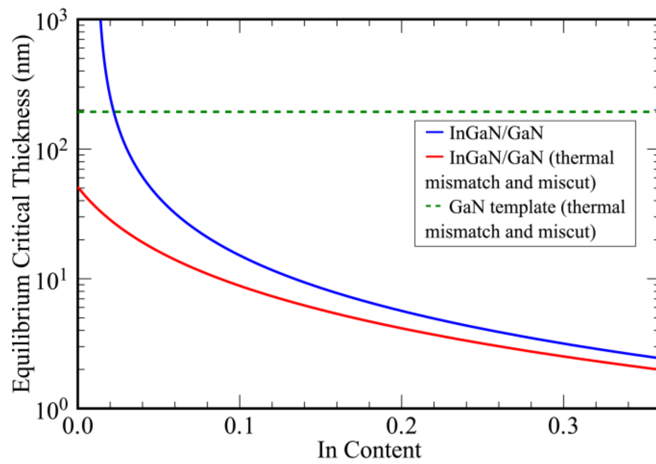

Figure 9: Energy-balance critical thickness calculations considering glide on the 1/3 <11-23> {1-101} slip system in $In_xGa_{1-x}N$ epilayers with varying In contents, subjected to a miscut sapphire substrate and thermal mismatch.

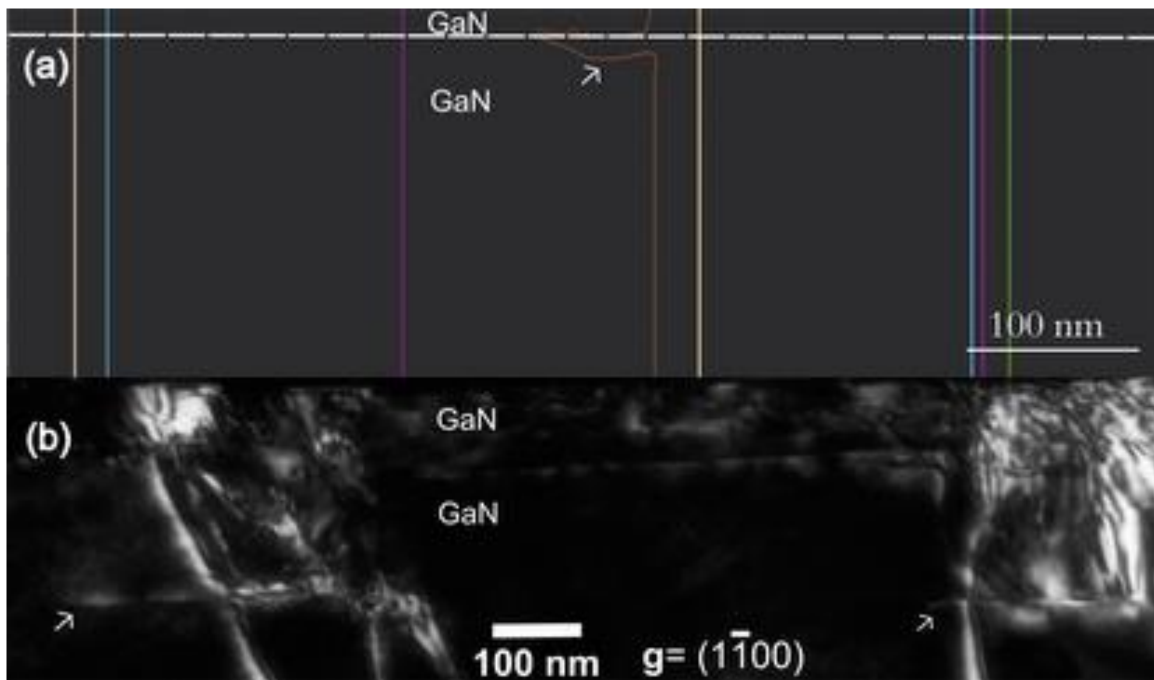

Figure 10: (a) Simulated dislocation microstructure using the PANIC dislocation dynamics model correlating well with (b) a WBDF **g**(2**g**) TEM image for sample D activating **g** = (1-100). The arrows show sub-interfacial defects.